

Thermal emission spectra of the ultra-hot Jupiter WASP-33 b

Qianyi Zou(邹乾一)^{1,2,3}, Meng Zhai(翟萌)^{1,3}, Wei Wang(王炜)^{1,3*}, Guo Chen(陈果)^{1,4}, Enric Pallé^{1,5}, Fei Yan(燕飞)^{6,7}, Huan-Yu Teng(滕环宇)¹, Qinglin Ouyang(欧阳青林)^{1,6}, Yaqing Shi(石亚卿)⁸, Li Zhou(周丽)¹, Zewen Jiang(姜泽文)⁹, Yujuan Liu(刘玉娟)^{1,3}, Thomas Henning¹⁰, Nicolas Crouzet¹¹

¹ National Astronomical Observatories, Chinese Academy of Sciences, Beijing, 100101, PR China

² Instituto de Astrofísica de Canarias, 38205 La Laguna, Tenerife, Spain

³ School of Astronomy and Space Science, University of Chinese Academy of Sciences, Beijing, 100049, PR China

⁴ CAS Key Laboratory of Planetary Science, Purple Mountain Observatory, Chinese Academy of Sciences, Nanjing, 210023, PR China

⁵ Departamento de Astrofísica, Universidad de La Laguna, 38206 La Laguna, Tenerife, Spain

⁶ Department of Astronomy, University of Science and Technology of China, Hefei 230026, PR China

⁷ Deep Space Exploration Laboratory, Hefei, Anhui 230026, China

⁸ Department of Science Research, Beijing Planetarium, Beijing, 100044, PR China

⁹ State Key Laboratory of Particle Astrophysics, Institute of High Energy Physics, Chinese Academy of Sciences, Beijing 100049, China

¹⁰ Max Planck Institute for Astronomy, Max Planck Institute for Astronomy, Königstuhl 17, D-69117 Heidelberg, Germany

¹¹ Kapteyn Astronomical Institute, University of Groningen, P.O. Box 800, 9700 AV Groningen, The Netherlands

Received 10 11, 2025

ABSTRACT

Observations of exoplanetary atmospheres provide critical insights into their chemical composition, formation and evolution history. Ultra-hot Jupiters serve as excellent targets for atmospheric characterization; studies of these planets may yield key understanding of gas giant's formation and evolution history. We present a thermal emission study of WASP-33 b's dayside atmosphere, based on two secondary eclipse observations with CFHT/WIRCam in two specific narrow band filters, namely the CO and CH₄_{on} filters, and archival data with HST/WFC3 and Spitzer. Stellar pulsations of the host star induce some quasi-periodic photometric variations, particularly in the CH₄_{on} band, which are modelled and corrected in the high-precision differential light curves. An eclipse depth of 1565.2^{+228.6}_{-237.5} ppm and 914.3^{+56.1}_{-57.0} ppm is determined for the CO and CH₄_{on} bands, respectively. Combined with HST/WFC3 and Spitzer data, our joint retrieval of WASP-33 b's dayside atmosphere reveals a high metallicity ([Fe/H] = 1.52^{+0.35}_{-0.52}), high C/O ratio (C/O = 0.78^{+0.03}_{-0.04}), and a thermal inversion layer, suggesting a formation history involving metal-rich gas accretion. We confirm the presence of the molecules H₂O, H⁻ and CO, and report a tentative detection of TiO in the dayside atmosphere of WASP-33 b. Future higher precision observations with JWST may provide better understand constraints on the chemical abundances of oxygen and refractory element abundances to better WASP-33 b's formation and evolutionary pathway.

Key words. Methods: data analysis - Techniques: photometric - Techniques: spectroscopic - Planets and satellites: atmospheres - Planets and satellites: formation - individual: WASP-33 b

1. Introduction

Characterizations of exoplanetary atmospheres are vital for addressing some key questions in the field of exoplanets, such as the formation and evolution of planets, the property and evolution of planet atmospheres, and the detection of possible biosignatures. Over the past two decades, atmospheric studies have predominantly focused on transiting close-in gas giants, par-

ticularly the hot Jupiters (HJs) and ultra-hot Jupiters (UHJs), thanks to their relatively strong atmospheric signals. Joint analysis based on data across broad wavelengths and/or multiple resolutions enable constraints on atmospheric temperature-pressure profiles, chemical composition, dynamics, and escape processes.

UHJs have high equilibrium temperatures $T_{\text{eq}} > 2200 \text{ K}$ (Parmentier et al. 2018; Stangret et al. 2022; Tan et al. 2024) and highly inflated atmospheres, which represent a distinct planet population and the most favor-

* E-mail: wangw@nao.cas.cn

able targets for time-resolved spectroscopic observations like transmission and emission spectroscopy (Snellen 2025). Recent abundance retrievals for some HJs and UHJs (e.g., WASP-121 b (Smith et al. 2024; Evans-Soma et al. 2025), WASP-18 b (Sheppard et al. 2017)) seems to be inconsistent with predictions for this population, particularly the expected inverse correlation between metallicity and the carbon-to-oxygen (C/O) ratio (Espinoza et al. 2017; Cridland et al. 2019). While mechanisms like pebble drift (Booth et al. 2017) could potentially explain these abundances, the observed discrepancies invoke the demand for more observation input to test and refine the current theories.

Moreover, several UHJs show significant spin-orbit misalignments, including MASCARA-5 b (Stangret et al. 2021), KELT-18 b (Rubenzahl et al. 2024), TOI-1518 b (Cabot et al. 2021), KELT-9 b (Gaudi et al. 2017), WASP-121 b (Delrez et al. 2016), WASP-33 b (Watanabe et al. 2022), indicating UHJs experiencing dynamically extreme evolutionary histories, such as eccentric *Lidov-Kozai* effect (Naoz et al. 2011). Atmospheric studies of these systems may therefore help constrain when and where planetary migration occurred.

UHJs experience stellar irradiation 10-100 times stronger than classic HJs, and 2-6 orders of magnitudes stronger than the warm or cool planets. The intense UV flux drives high temperatures that produce thermal inversions in their upper atmospheres (Baxter et al. 2020). Within and above the temperature inversion layer on the dayside, most molecules like H_2O , TiO and VO undergo thermal dissociation, while CO can still remains relatively abundant (Madhusudhan 2012; Moses et al. 2012; Drummond et al. 2019). Therefore, atmospheres become dominated by atomic and ionic species (e.g., Fe I/II , Mg I , Ca II , Na I , Ti I and V I).

Observations from ground-based HRS and space-based low-to-medium resolution spectroscopy support the transition from molecular to atomic and ionic species in UHJs, reflecting extensive thermal dissociation at high temperatures, although nightside cold-trapping and rainout at the terminator that has been observed (Gandhi et al. 2023; Hoeijmakers et al. 2024) may also play a role. Some UHJs exhibit extended envelopes or tails as revealed from transit or near-transit observations, suggesting extreme mass loss (Yan & Henning 2018; Cabot et al. 2020; Yan et al. 2021). These observational atmospheric properties are highly valuable for understanding composition of UHJ's atmosphere and refining 3D atmospheric modeling with General Circulation Models (GCMs).

WASP-33 b, a transiting UHJ discovered by Christian et al. (2006) in the SuperWASP project (Pollacco et al. 2006), has an orbital period of ~ 1.22 days. Follow-up observation measurements yielded a mass of $2.1 M_{\text{J}}$ and a radius of $1.6 R_{\text{J}}$ (Chakrabarty & Sengupta 2019). Notably, its host star WASP-33 (HD 15082) is a bright rapidly rotating A5 δ Scuti star (Grenier et al. 1999; Cutri et al. 2003), making it a peculiar exoplanet. Subsequent *Rossiter-McLaughlin* effect (RME) observations (Johnson et al. 2015; Stephan et al. 2022; Watanabe et al. 2022) revealed a near-polar orbit, showing strong resemblance to two other UHJs around A-type stars, i.e., KELT-9 b (Gaudi et al. 2017) and WASP-189 b (Anderson et al. 2018; Lendl et al. 2020). This configuration suggests an intense migration history potentially involving mechanisms like eccentric *Lidov-Kozai* effects (Naoz et al. 2011). Interestingly, Mugrauer (2019) pointed out that WASP-33 is at least a binary or even a hierarchical triple star system, including a close-in M-dwarf companion (WASP-33B, $\rho \sim 1.9''$, $\Delta K_s = 6.11 \pm 0.02$) (Moya et al. 2011; Wöllert & Brandner 2015; Ngo et al.

2016) and a wide-separation G-dwarf companion (WASP-33C, $\rho \sim 49.0''$; Mugrauer 2019), invoking the possibility of dynamic perturbation on the planet in the past and/or still ongoing.

Multi-resolution studies across broad wavelength range have been conducted extensively for the characterization of WASP-33 b. Early photometric eclipse measurements at $0.91 \mu\text{m}$, the K_s band and the Spitzer/IRAC broad band yielded notably high dayside brightness temperatures ($\geq 3300 \text{ K}$), suggesting a potential thermal inversion supported or a high C/O ratio (Smith et al. 2011; Deming et al. 2012; De Mooij et al. 2013). The first eclipse spectrum, obtained by Haynes et al. (2015) using HST/WFC3, showed excess flux at short wavelengths that was attributed to TiO emission. However, subsequent reanalysis of this data by Changeat et al. (2022) and High Resolution (HR) spectroscopy have questioned TiO 's presence (Nugroho et al. 2017; Cont et al. 2021; Herman et al. 2020; Yang et al. 2024a). Recent optical and NIR HR spectra detected atomic species, including Fe I (Nugroho et al. 2020), Si I (Cont et al. 2022), V I and Ti I (Cont et al. 2022), molecules, including CO (van Sluijs et al. 2023; Yan et al. 2022), OH (Nugroho et al. 2021) and weak H_2O signal (Nugroho et al. 2021), revealing thermal inversion and strong dissociation on the dayside. Transmission spectroscopy detected absorptions from Ca II (Yang et al. 2024a) and AlO (von Essen et al. 2019), and probed an extended envelope with escape rate of $\sim 10^{12} \text{ g s}^{-1}$ via measuring additional absorption of Balmer lines. Notably, Yang et al. (2024b) identified a possible contribution from nightside H_2O emission in the transmission spectra, suggesting the presence of nightside water and that WASP-33 b may exhibit non-isothermal temperature structures on its nightside. Phase-curve observations reveal inefficient day-night heat redistribution (Zhang et al. 2018; Herman et al. 2022; Dang et al. 2024) and CO absorption on the nightside, making WASP-33 b the second exoplanet with confirmed nightside molecules (Mraz et al. 2024). However, most constraints remain limited to species detection, with few atmospheric retrievals conducted (Haynes et al. 2015; Changeat et al. 2022; Finnerty et al. 2023). These retrievals consistently indicate a dayside thermal inversion, as predicted by Mollière et al. (2015) for atmospheres with $\text{C/O} \approx 1$ and $\text{Teff} \gtrsim 1500 \text{ K}$, yet they differ in molecular abundances and profile details, highlighting atmospheric complexity that requires further observational constraints.

In this work, we report two ground-based high-precision eclipse observations of UHJ Jupiter WASP-33 b obtained with CFHT in 2015 using the CH_4on filter and our customized CO filter. Section 2 details the observational setup, followed by a brief description of data reduction and analysis in Section 3. Section 3.5 describes our atmospheric retrieval methodology and results, following by the summary in Section 5.

2. Observations

We observed two secondary eclipses of WASP-33 b (Program 15AS007; PI: Wei Wang) using the Wide-field InfraRed Camera (WIRCam)¹ on the Canada-France-Hawaii Telescope (CFHT). WIRCam features a $21 \text{ arcmin} \times 21 \text{ arcmin}$ field of view that enables differential photometry with multiple reference stars. Observations occurred on 25 October 2015 in the CO filter (5.2 hours duration) and 24 December 2015 in the CH_4on filter (6 hours duration). As Fig. 1 shows, both of them fully covered the secondary eclipse along with ~ 2.5 hours of out-of-eclipse baseline. We acquired 696 exposures (12s each) in CO and 996 expo-

¹ <https://www.cfht.hawaii.edu/Instruments/Imaging/WIRCam/>

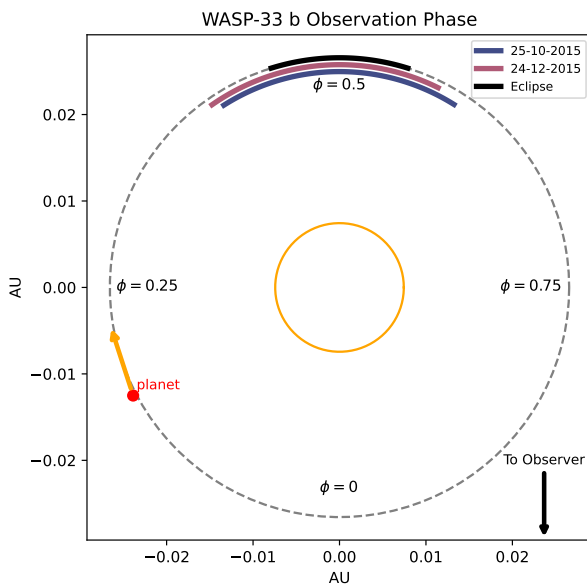


Fig. 1: The orbit phases of our two observations. Specifically, Night 1 covered phase 0.410–0.589 (October 25 2015), Night 2 covered phase 0.403–0.573 (December 24 2015).

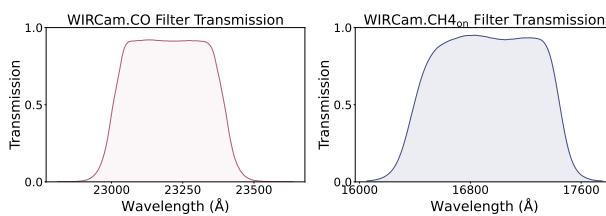


Fig. 2: The transmission curves of the CO and CH_4_{on} filters used in this work.

ures (3.5s each) in CH_4_{on} . In order to achieve differential photometric precision to 10^{-4} , the 'Staring Mode' (Devost et al. 2010) was used in both observations, following the previous successful attempts (e.g., Croll et al. 2010; Wang et al. 2013; Chen et al. 2014; Shi et al. 2023). The 'Staring Mode' aims to maintain the telescope's pointing stability to less than a few pixels, thereby minimizing the impact of intrapixel and interpixel variations of the detectors on photometric precision. However, our data show the target star exhibits large movement with maximum shifts of ~ 15 pixels in the CO filter. This drift likely results from the guiding system misidentifying a cluster of hot pixels on Detector #77 as a stellar point during observations. The misidentification also leads to World Coordinate System (WCS) interpretation failures for the affected frames, rendering them unusable. In contrast, target movement remains within 5 pixels in the CH_4_{on} filter. Figure. 2 shows the filter information of CFHT/WIRCam's CO and CH_4_{on} filters, whose λ_{mean} are 2.32 μm and 1.69 μm . The CO filter is customized to be sensitive to CO feature at about 2.3 μm , while the CH_4_{on} filter is sensitive to both CH_4_{on} and H_2 . We use these two filters to assess the presence and abundances of CO, CH_4_{on} and H_2 , and thus to provide constraints on the C/O ratio and metallicity.

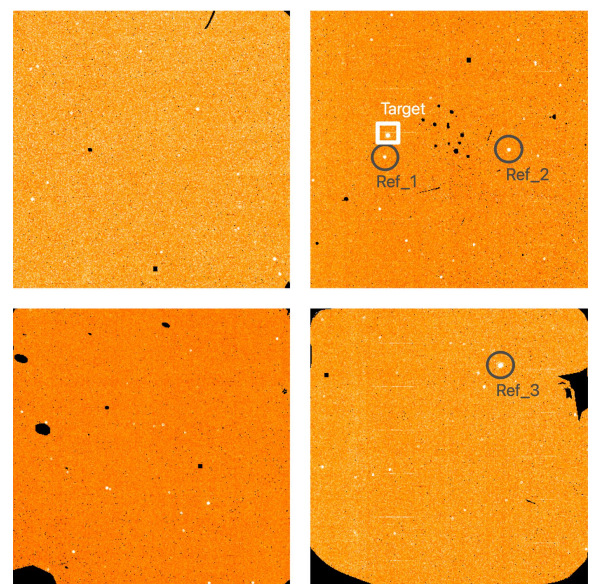


Fig. 3: The CO filter reduced full-frame WIRCam image of WASP-33 taken on 25 October 2015. The target star is marked as the white square and the final chosen reference stars are marked as the grey circles.

3. Data Analysis

3.1. Raw data Reduction and Correction

Observations obtained with CFHT/WIRCam utilized the sample-up-the-ramp (non-destructive readout) mode (Finger et al. 2008), with each integration sequence consisting of 12 reads. Our analysis reveal that the initial read of each sequence on Detector #52 consistently exhibited elevated counts, producing photometric values 1.002–1.004 times higher than the median of other reads, which can not be corrected reliably. Hence, we excluded the first read of each sequence and only used the remaining 11 reads in this work.

The raw data were reduced by the 'I'iwi pipeline (version 2.1.200)², including flagging the saturated pixels, non-linearity correction, reference pixels subtraction, dark subtraction, flat fielding, bad pixels masking and guide window masking. Technically, the 'I'iwi pipeline should assign bad pixels and saturated pixels's count a value of Not-a-Number (NaN). However, we find that several pixels within the stellar profile are misclassified as saturated pixels by 'I'iwi, resulting in their assignment of NaN values. This misclassification further exacerbates challenges associated with our data reduction and analysis. Figure. 3 shows a full-frame CO filter's reduced image illustrating our observation FOV, in which the target star is marked as the red square and the final chosen reference stars are marked as the blue circles.

As shown in Fig. 3, the WIRCam detectors contain a large number of bad pixels. While reference stars were preferentially selected to avoid regions with clustered bad pixels, there are still some isolated defective pixels occasionally remaining within photometric apertures of some references stars in some exposures, leading to strong systematic in the yielded lightcurves and thus preventing a high-precision differential photometry. To mitigate this effect, we employed the `Background2D` module from

² <https://www.cfht.hawaii.edu/Instruments/Imaging/WIRCam/IiwiVersion2Doc.html>

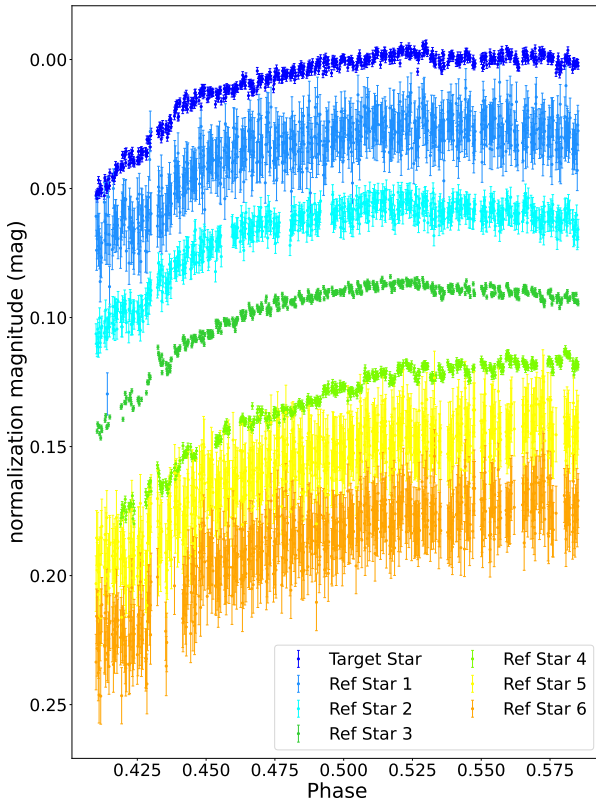


Fig. 4: Normalized light curves of target star and the candidate reference stars.

the Photutils package (Bradley et al. 2024) for spatial interpolation of the NaN values, following the methodology outlined by Ding et al. (2025). This technique can estimate the data values for the affected pixels, demonstrating reliable performance in handling such detector imperfections.

3.2. Photometry and light curve determination

To achieve a photometric precision down to 10^{-4} that is required for the characterization of exoplanet atmospheres, our observation were carried out in defocused mode. With this configuration, the observation efficiency is maximized to gain more photons in the eclipse, and the uncertainties in flat-fielding, intrapixel and interpixel sensitivity variations are minimized. The disadvantage of such a setup is that the PSF (point spread function) of a star become donuts-shaped rather than gaussian-shaped. In our case, the resulting PSF has a radius of $\sim 10-15$ pixels. We have developed a new pipeline written in Python, based on and improved from the IDL pipeline used in Shi et al. (2023). Our pipeline employs a parallelized processing approach, reducing the photometry and light-curve modeling time for a single band from ~ 1 day to ≤ 40 minutes.

We followed the high-precision differential aperture photometry algorithm firstly proposed by Everett & Howell (2001) and developed by Croll et al. (2010); Wang et al. (2013); Shi et al. (2023) for the data reduction, light curve detrending and final light curve determination. We initially selected all stars with comparable brightness ($\Delta m < 2.5$ mag) within the FOV as candidate reference stars, preferentially selecting those located within the same detector that the target star resides. To ensure photometric coherence, we further exclude those candidates exhibiting

Table 1: Parameters for the WASP-33 b system

Property	Value	References
WASP-33		
Property	Value	References
RA	02:26:51.06	[1]
DEC	+37:33:01.7	[1]
Spectral Type	A5	[2]
J_{band} (mag)	7.58	[3]
K_{band} (mag)	7.47	[3]
Radius (R_{\odot})	$1.602^{+0.062}_{-0.055}$	[4]
Mass (M_{\odot})	$1.653^{+0.350}_{-0.187}$	[4]
T_{eff} (K)	7308^{+133}_{-109}	[4]
Metallicity (dex)	0.1	[5]
WASP-33 b		
Period (d)	$1.219870 \pm 1 \times 10^{-6}$	[6]
T_0 (d)	$2454163.223670 \pm 0.00022$	[6]
a/R_{\ast}	3.571 ± 0.010	[6]
R_p (R_J)	1.593 ± 0.074	[6]
i ($^{\circ}$)	86.63 ± 0.03	[6]
Mass (M_J)	2.093 ± 0.139	[6]

Notes. [1]Gaia Collaboration (2020)[2]Grenier et al. (1999)[3]Cutri et al. (2003)[4]Stassun et al. (2019)[5]Zhang et al. (2018)[6]Chakrabarty & Sengupta (2019)

the out-of-eclipse light curves not similar with that of WASP-33 and other references (e.g., the Ref Star 4 in Fig.4), as such discrepancies suggest the star may be intrinsically variable and thus unsuitable as a reference. Unfortunately, WASP-33 is so bright that there are only a few (≤ 8) qualified candidates for each filter.

For all the selected candidate reference stars, the raw light curves for a given photometry aperture diameter (D) were derived and normalized using the median values derived from a $2-3\sigma$ clipping algorithm. Then, we performed systematic quality screening on the light curves and time-series data points. As exemplified by the CO filter data in Fig.4, the first 1,700s data (phase 0.410-0.426) exhibited degraded quality and were hence excluded. The Ref4 candidate displayed obviously divergent photometric trends compared to the target star and other reference stars, and was thus discarded from reference star list. Similar approach was applied to CH_4on filter data, with slightly modified criteria: both the initial and final 960s data (phase 0.403-0.412 & 0.564-0.573) were removed due to notable worse data quality. These two excisions somewhat reduced the amount of out-of-eclipse baseline data but improved the overall data quality and reduced the scatter.

Then, an average reference light curve for a given aperture D and reference star group (RSG), denoted as $L_{\text{ref}(D,\text{RSG})}$, was obtained by taking the weighted mean of the normalized light curves with weights proportional to the inverse variance of their photometric uncertainties ($w_i \propto 1/\sigma_i^2$); this averaged light curve was then used to divide the target light curve so that most systematics were removed. Finally, a 3σ clipping algorithm is applied to remove obvious outliers in the normalized target light curve.

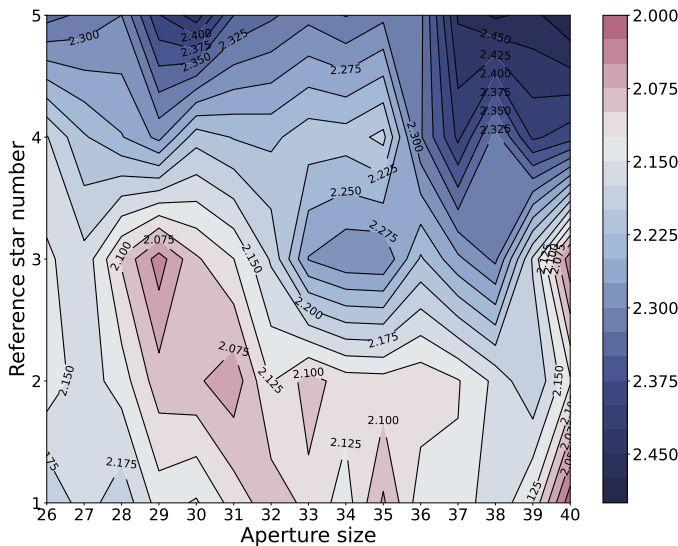


Fig. 5: Contour maps of the normalized $\text{rms} \cdot \beta^2$ distribution are superimposed on the two-dimensional parameter space defined by D and N_{RSG} in the CO filter data. The pixel scale is $0.306 \text{ arcsec pixel}^{-1}$. The minimum value of $\text{rms} \cdot \beta^2$ is reached with $D = 29$ and $N_{\text{RSG}} = 3$.

The derived target light curves are modelled using `batman` (Kreidberg 2015), with modeling parameters summarized in Table 1. To provide a reasonable reference for the eclipse depths in the CO and CH₄_{on} filters, we built a forward model of WASP-33 b's dayside atmosphere with `petitRADTRANS` (Mollière et al. 2019) using the retrieval results of Finnerty et al. (2023), and then compared the modeled planetary spectrum to the host star's stellar spectrum; accounting for the filters' bandwidths and transmission profiles with the species (Stolker et al. 2020) yielded the reference eclipse depths. While background-related polynomial baseline of the NIR secondary eclipse light curves have been widely reported (Croll et al. 2010; Wang et al. 2013; Chen et al. 2014; Shi et al. 2023), we did not detect such features in our data. This absence is likely attributed to the dominant influence of WASP-33's pulsations, which may significantly overshadow instrumental or background effects.

3.3. Finding the 'best' light curve

It is well recognized in our previous work and literature that for almost every combination of D and RSG, the obtained light curve can be fitted with an eclipse-wise light curve plus various noises, with slightly different eclipse depths, uncertainties and best-fitting residuals. This highlights the necessity to find the 'best' combination of D and RSG, which gives the 'best' light curve that has the smallest fitting residuals while no noticeable hint for overfitting. To do so, we follow the methodology described in Shi et al. (2023), developed from Croll et al. (2015). The key idea of this method is to find a balance between underfitting and overfitting, by combining the two parameters, rms and β , whereas rms is the root-mean-square of the residual light curve after subtracting the best-fit model, and β is the ratio of the residuals to the Gaussian noise expectation as defined in Winn et al. (2008). The method to derive β is described in details in Section 3.5.

When the photometric aperture D encompasses a region where stellar photons dominate over the sky background, the residual rms tends to decrease with increasing D , gradually approaching the optimal aperture. However, as D continues to grow and the aperture begins to include the outer regions of the stellar profile, red noise becomes increasingly non-negligible. This leads to a flattening of the rms curve near its minimum or a slow upward trend. In such cases, the β factor amplifies subtle variations in rms, helping to distinguish and exclude aperture choices with comparable rms values that are affected by correlated noise. Therefore, we use rms and β as proxies to achieve a balance between the two competing parameters. In practice, for each set of RSG and D , we derive the differential target-to-reference-assembly light curve. The next step is to model all (if possible) systematics (or correlated noises) embedding in the derived light curve, and remove them, to achieve a reliable and high-precision eclipse and the minimum rms and β . After that, we will obtain a $\text{rms} \cdot \beta^2$ 2D grid, which is smoothed and a minimum value of $\text{rms} \cdot \beta^2$ can thus be located.

For the case of WASP-33 b, one additional approach has to be performed, which is to model and remove the relatively strong stellar pulsation observed in WASP-33. Fortunately, the pattern of the stellar pulsation seems to be irrelevant to the selection of RSG and D , and therefore is left to be corrected afterwards.

In Fig. 5, an $\text{rms} \cdot \beta^2$ contour map for the CO filter as functions of D and N_{RSG} is shown, where the minimum is achieved at $D = 29$ pixels and $N_{\text{RSG}} = 3$. We use the same aperture size for the target and reference stars at this stage, but then perform subsequent refinement by individually varying D for each reference star and the target with ± 1 pixel increments, yielding final apertures of $D = 29$ pixels for the science target and $D = 28, 39, 39$ pixels for the 3 reference stars.

Similar approaches have been applied for the CH₄_{on} filter data. However, WASP-33's is so bright in this band so that there are only few usable reference stars (Fig. 6), resulting in the optimal $N_{\text{RSG}} = 1$ and $D = 33$ pixels. The final-chosen apertures are $D = 29$ and 30 pixels for the target and reference star, respectively.

It is worthy to note that in both the CO and CH₄_{on} band observations, there seem to be instrumental anomalies in some non-destructive readouts, in which all the 12 sub-integrations show 5σ deviations from the nearby readouts; these outliers are flagged and excluded from model fitting.

As noted in Section 1, the WASP-33 system may be a triple-star system (Mugrauer 2019). Although the M dwarf companion (WASP-33 B) can be spatially resolved by a 4m class telescope, it is complicated for our WIRCam observation due to the defocus setup and thus a widespread PSF. Therefore, partial contamination may occur. We thus carefully examined the raw images in both filters but found no hint of WASP-33 B near its expected position, possibly due to the large magnitude difference of ~ 6.11 mag in K_s and the very short exposure time. Following Shi et al. (2023), we quantified the M-dwarf's contaminating signal and found it contributes only a few ppm to the eclipse depth – far below the measurement uncertainty. The other even fainter companion is quite far away with an angular separation of $\sim 49.0''$ and thus can be ignored without any risk. We therefore find no evidence for companion-induced contamination in our photometric data and no contamination correction was applied.

3.4. Suppression of stellar pulsation

WASP-33 b is a rare exoplanet orbiting a variable star. The host star HD 15082, a δ Scuti type star, exhibits a dominant pulsation with period of $\sim 20 \text{ days}^{-1}$ and a maximum amplitude of

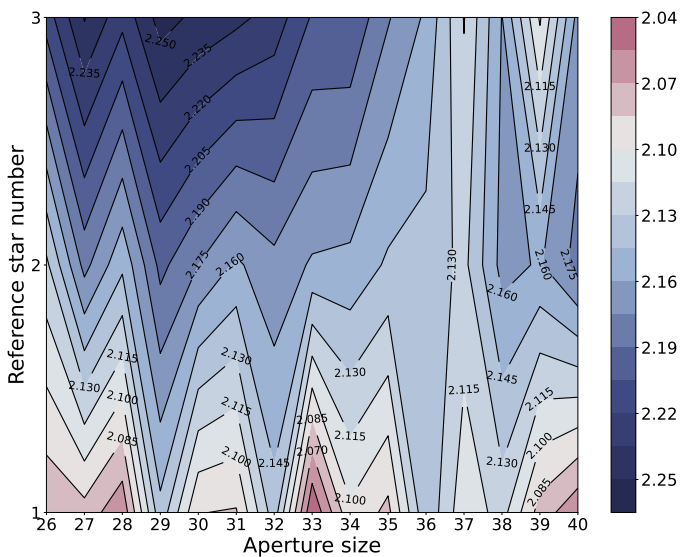


Fig. 6: Same as Fig.5 for the CH₄_{on} filter. The minimum value of rms* β^2 is reached with $D = 33$ and $N_{RSG} = 1$.

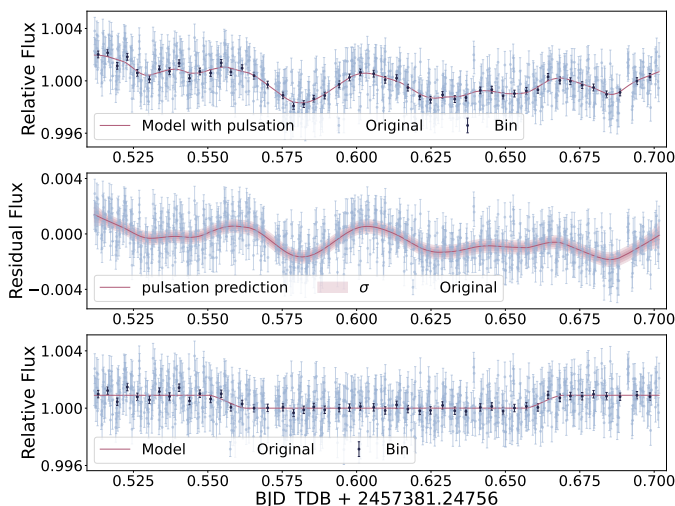


Fig. 7: Pulsation noise removal plot for CH4_{on} filter's data. The upper panel illustrates photometric measurements contaminated by pulsational noise, depicted as light points(unbinned) and dark points(binned). A synthesized baseline model(red curve) combines the eclipse signal generated with batman and the pulsational signature predicted by celerite2. The middle and lower panels respectively present the extracted pulsational component and the corrected eclipse light curve after systematic noise removal.

~ 1.5 mmag (von Essen et al. 2014). This pulsation may significantly compromise the accuracy of eclipse depth measurements, and therefore must be modelled and removed.

By analyzing the TESS Sector 18 data, Von Essen et al. (2020) identified 29 stellar pulsation frequencies with signal-to-noise ratios (SNR)>4 in WASP-33. However, Baluev & Sokov (2025) demonstrated that the stellar pulsations may evolve on multi-year timescales after including the TESS Sector 58 data. We have tried using the pulsation models derived from Baluev & Sokov (2025) and Von Essen et al. (2020) to mitigate the notable photometric variations in the obtained light curves, but the remaining residuals are still non-negligible and bear

some patterns. Deming et al. (2012) were able to mitigate the stellar pulsations by combining long-baseline ground-based observations with nearly contemporaneous Spitzer data, enabling the identification of relatively stable pulsation periods that could be modeled and removed from the light curves. In our case, however, the available baseline is considerably shorter, the CFHT and Spitzer observations are widely separated in time, and the pulsation properties of WASP-33 are known to vary. Under these circumstances, applying a similar approach would likely require fitting a large number of additional parameters and may therefore not be practical.

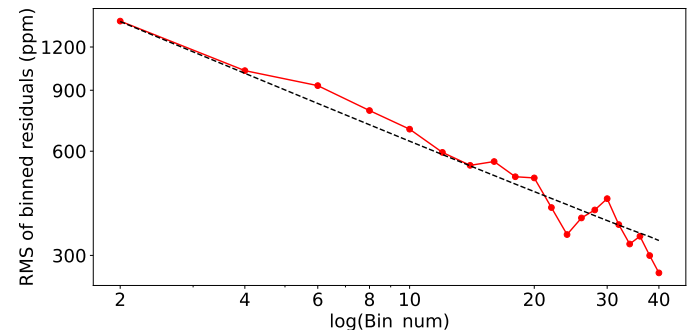


Fig. 8: Comparison of data-model residuals and theoretical noise levels across varying bin sizes in CO filter.

Therefore, we follow Zhang’s method (Zhang et al. 2018) by employing Gaussian Process (GP) to fit these pulsations nonparametrically with the public GP code `celerite2`, (Foreman-Mackey et al. 2017; Foreman-Mackey 2018). The core of this method is that GP can treat pulsations as a combination of various noises whose properties can be described by a parameterized covariance matrix fitted to data. By removing the requirement to prescribe a mathematical form to the oscillations, this method enables non-stationary oscillatory behavior throughout the observations. The `celerite` framework constructs the covariance matrix through a kernel function exclusively parameterized by the temporal separation $|\tau = t_i - t_j|$. The kernel used here consists of two radial functions, inspired by simple harmonic oscillator, augmented with a diagonal component to account for the white noise, which is:

$$k(\tau) = S_0 \omega_0 Q e^{-\frac{\omega_0 \tau}{2Q}} (\cos(\eta \omega_0 \tau) + \frac{1}{2\eta Q} \sin(\eta \omega_0 \tau)), \quad (1)$$

where $\eta = |1 - (4Q^2)^{-1}|^{\frac{1}{2}}$.

Two sets of kernels are combined together to model the stellar pulsations. In the first kernel, all the three parameters (Q, S_0, w_0) are allowed to vary in the fit, while in the second kernel, Q is fixed to $1/\sqrt{2}$, only S_0, w_0 are free parameters. These two kernels represent the oscillatory component and the non-oscillator component that decays rapidly with τ of stellar pulsations, respectively. In addition, we incorporate the eclipse depth as another free parameter in the fitting process to mitigate potential covariance with the forward model assumptions. For the CH₄_{on} band data, the broader bandwidth returns higher SNR, enabling quite robust identification and systematic removal of pulsation-induced noise, as illustrated in Fig. 7. Conversely, the pulsation correction in the CO band is less successful, due to the narrower bandwidth and limited data volume and thus suppressed pulsation signatures.

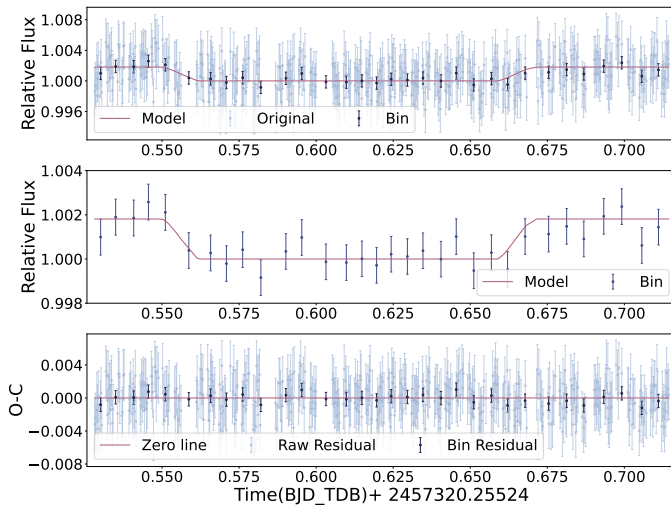


Fig. 9: Secondary eclipse of WASP-33 b observed by CFHT/WIRCam in the CO filter on Oct 25, 2015. The top panel displays the unbinned (light-shaded points) and binned (dark-shaded points) light curves overlaid with the best-fit secondary eclipse model (red solid line). The middle panel isolates the binned data alongside the optimized eclipse model, while the bottom panel presents the residuals relative to the model fit. The rms of the binned residuals is 544.9 ppm.

3.5. Light curve rebinnning and fitting

Till now, the photometric precision of each data point of the obtained light curve is $\sim 10^{-3}$, the same order of magnitude with the eclipse depth of a typical HJ. To obtain a robust determination of the eclipse depth, rebinnning data points before light curve fitting is essential. While the $rms \cdot \beta^2$ method can identify an optimal bin size together with an optimal $L_{ref}(RSG, D)$, this initial binning is on the light curves obtained using identical D for both the science target and the references stars, and they still remain contaminated by pulsation noise. After finalizing individual D values for every stars and removing pulsation contamination, the bin size for each band is re-optimized.

As described previously, we employ the β parameter (Winn et al. 2008) to quantify the level of correlated noise. Taking the CO filter data as an example, β is calculated by averaging ratios across bin sizes ranging from 2 to 40 data points (with upper limit set to ensure time sampling size to be less than WASP-33 b's ingress/egress duration; see Fig. 8). The unphysical cases where the scaled-down residuals fall below Gaussian noise expectations, i.e., $\beta < 1$, are discarded. After this evaluation, a bin size of 14 is adopted for the CO filter data. A similar procedure yields a bin size of 18 for the CH4_{on} filter data.

The rebinned CO and CH4_{on} band light curves, as shown in the middle panels of Figs 9&10, are used to determine final eclipse depths via Markov Chain Monte Carlo (MCMC) analysis using the emcee package (Foreman-Mackey et al. 2013). The MCMC sampling is performed on two parameters, the eclipse depth distributed uniformly, and the central eclipse time T_{mid} distributed normally with sigma being the error of T_{mid} , propagated from the uncertainty quoted in Zhang et al. (2018). Each parameter is sampled with 6 walkers. An initial 1000-step run refines parameter guesses, followed by a final 6000-step sampling with 12 walkers and a step size of $10^{-8} > 50$ times of the best-fit binned data length to avoid possible autocorrelation. After discarding the first 20% of the chains as burn-in, we con-

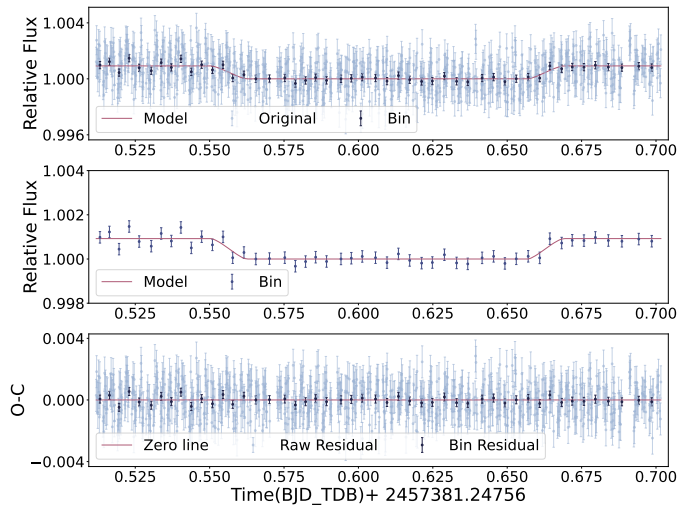


Fig. 10: Secondary eclipse of WASP-33 b observed by CFHT/WIRCam in the CH4_{on} filter on Dec 24, 2015. Same as Fig.9. The rms of the binned residuals is 217.1 ppm.

firmed that the acceptance rates remained within 20%–50%, consistent with appropriately chosen step sizes. Convergence was further assessed using the Gelman–Rubin statistic (R), which was found to be close to unity for all parameters. The best-fit eclipse depths in the CO and CH4_{on} bands are $1565.2^{+228.6}_{-237.5}$ ppm and $914.3^{+56.1}_{-57.0}$ ppm, respectively (see Fig.11).

3.6. Modelling

In addition to our newly obtained CFHT/WIRCam CO and CH4_{on} band measurements, for the dayside atmosphere investigation, we collected the HST/WFC3 emission spectrum obtained by Haynes et al. (2015) and the Spitzer/IRAC 3.6 and 4.5 μ m photometric eclipse depths obtained by Zhang et al. (2018); Dang et al. (2024). In total, we have 13 eclipse depth measurements spanning from 1.1 μ m to 4.5 μ m. Note that two HST data points are excluded, as explained in Sec 4.1.

We employ the petitRADTRANS package (Mollière et al. 2019; Nasedkin et al. 2024) and construct two atmospheric models: a free-chemistry (FREE) model and an equilibrium chemistry (EQ) model. The python package PyMultiNest is used to explore the posterior distribution and calculate the Bayesian evidence (Buchner et al. 2014), which implements the multi-modal nested sampling algorithm based on the MultiNest library (Feroz et al. 2009).

For the FREE model, we assume a one-dimensional atmospheric structure with a temperature inversion layer spanning a pressure range of 10^{-6} to 10^3 bar, divided into 100 uniformly spaced layers in logarithmic space. Previous HR study indicates that the temperature of the upper atmosphere is lower than that of the inversion layer (Haynes et al. 2015; Nugroho et al. 2017; Herman et al. 2020; Finnerty et al. 2023), which means the commonly adopted 2-point T-P profile (Buchner et al. 2014) is inadequate. We therefore introduce a third point (T₃, P₃). Unlike the 3-point T-P profile proposed by Waldmann et al. (2015), we fix P₃ at 10^{-6} bar rather than treating it as a free parameter. Based on the previous studies on WASP-33 b's dayside, we include CO (Rothman et al. 2010), H₂O (Rothman et al. 2010), CH₄ (Yurchenko et al. 2017) and TiO (McKemmish et al. 2019), which possess prominent spectral features in the wavelength

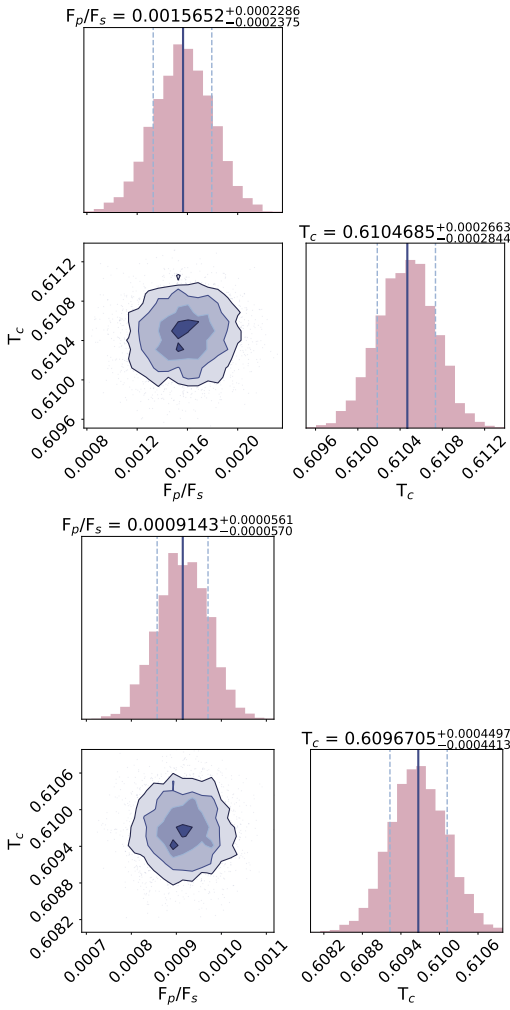


Fig. 11: Best-fit parameters of the binned light curve for the CO (Upper) and CH_4on (Lower), with $T_{\text{mid}} = T_c - 57319.75524$ and $T_{\text{mid}} = T_c - 57381.24756$.

coverage of interests. We have not included OH - a photodissociation product of H_2O - in our model, due to the lack of OH sensitive features in the data set we use in this work. The mass fractions of these species are treated as free parameters, while H_2 and He serve as filler gases to maintain a total mass fraction, with a fixed He/ H_2 mass ratio of 0.305. Contributions from Rayleigh scattering by H_2/He and continuum absorption from $\text{H}_2\text{-H}_2$, $\text{H}_2\text{-He}$ and H^- are considered, and the inclusion of the latter necessitates treating the mass fractions of its associated species, e^- and H, as free parameters. Given the high temperatures on the dayside, the atmosphere is likely to be cloud-free, and thus no cloud prescription is included in the retrieval process. For the EQ model, we use the same 3-point T-P profile as described above. The free parameters to be explored are the C/O ratio and the metallicity [Fe/H]. Both retrieval models are initially computed at a spectral resolution ($\lambda/\Delta\lambda$) of 1,000 and subsequently binned to match the observational passbands. They share common fixed parameters, including planetary radius of 1.593 R_J , surface gravity of 27.114 m/s^2 and orbit semi-major axis of 0.02558 au.

To identify potential species from the obtained emission spectrum, we first computed the Bayesian evidence (Kass & Raftery 1995) for the full model(including all species). We then iteratively exclude one species at a time and recalculate the Bayes factors for each reduced model. Following the criteria

Table 2: Best-fit parameters from the FREE model retrieval on WASP-33 b

Parameter	Prior	Posterior distribution	Unit
T_1	$\mathcal{U}(1000, 3000)$	1345 ± 265	K
T_2	$\mathcal{U}(3000, 5000)$	4887 ± 110	K
T_3	$\mathcal{U}(1000, 3000)$	2641 ± 20	K
P_1	$\mathcal{U}(-2, 3)$	-1.50 ± 0.24	log bar
P_2	$\mathcal{U}(-6, -2)$	-3.91 ± 0.22	log bar
P_3	-6	...	log bar
H^-	$\mathcal{U}(-10, -1)$	-2.131 ± 0.073	dex
H	$\mathcal{U}(-10, -1)$	-5.5 ± 3.0	dex
e^-	$\mathcal{U}(-10, -1)$	-2.3 ± 0.94	dex
H_2O	$\mathcal{U}(-10, -1)$	-6.2 ± 2.5	dex
CO	$\mathcal{U}(-10, -1)$	-4.9 ± 2.9	dex
TiO	$\mathcal{U}(-10, -1)$	-6.6 ± 2.1	dex
CH_4	$\mathcal{U}(-10, -1)$	$-6.9n \pm 2.1$	dex

proposed by Kass & Raftery (1995), evidence strength is categorized as: strong ($|\Delta \ln \mathcal{Z}| \geq 5$), moderate ($3 \leq |\Delta \ln \mathcal{Z}| < 5$), weak ($1 \leq |\Delta \ln \mathcal{Z}| < 3$), or inconclusive ($|\Delta \ln \mathcal{Z}| \leq 1$).

4. Retrieval analysis

4.1. FREE model retrieval

The FREE retrieval analysis yields a best-fit spectrum that is largely featureless, with residuals exceeding 3σ at the blue-end data points (1.155 and 1.199 μm). These two points dominate the χ^2 value, leading to an in general poor fit.

Haynes et al. (2015) attributed the unusually large depths at 1.155 and 1.199 μm to a high abundance of TiO, yet subsequent joint retrievals (Changeat et al. 2022) combining HST and Spitzer data and later HRS studies have contested the presence of dayside TiO (Herman et al. 2020; Cont et al. 2021). To test this hypothesis, we ran several forward models with temperature inversion layers including only H, He and TiO, assuming different TiO abundances, and find that the TiO abundance must be $\geq 10^{-4}$ to account for the observed 1.155 and 1.199 μm depths. However, such high TiO abundance should lead the eclipse depths of the CH_4on and CO bands (especially the latter one) to be significantly higher than our measured depths, and TiO should be detected in the HR studies (Nugroho et al. 2017; Herman et al. 2020; Cont et al. 2021; Serindag et al. 2021).

We thus argue that the large 1.155 and 1.199 μm depths can not be due to a high TiO abundance. Rather, it should come from their imperfect pulsation signal correction. Haynes et al. (2015) noticed the pulsation signals in their lightcurves, and modeled pulsation signals by sine functions. However, such procedure was later found only capable of removing $\sim 10\%$ of the pulsation noise (Zhang et al. 2018), and thus leaving substantial pulsational residuals in at least some of the HST/WFC3 light curves. Given that WASP-33 is an A-type star, pulsational noise affects the precision of eclipse depth measurements much more significantly at shorter wavelengths, and thus the 1.155 and 1.199 μm depths should still be affected by pulsation noise. To mitigate this, and given that the two bluest data points are inconsistent

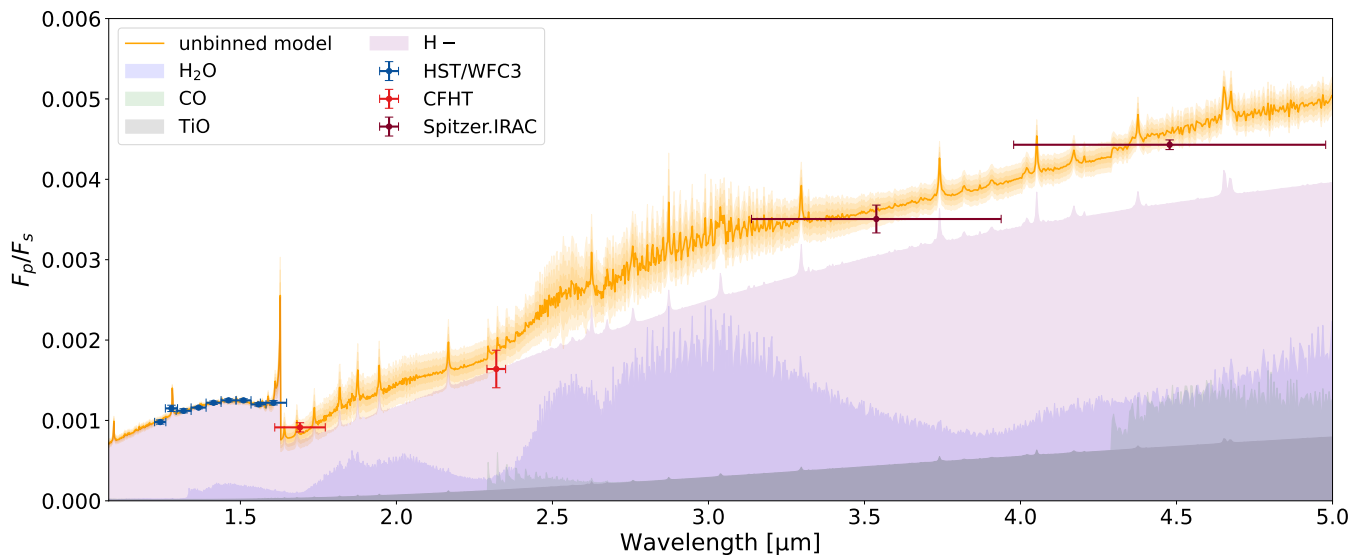


Fig. 12: Best-fit FREE model spectrum together with the data points from HST, CFHT and Spitzer shown in filled dots with error bars and distinct colors. The orange curve and surrounding shaded region represent the best-fit model and its 3σ regime. The shaded areas in different colors below the orange curve indicate the reference models containing only H_2O , CO , TiO or H^- , respectively.

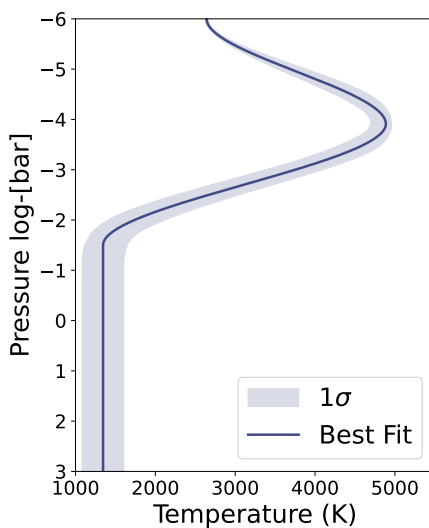


Fig. 13: Retrieved temperature-pressure (T-P) profile for the FREE model. The solid blue line shows the best-fit solution, and the shaded area denotes the 1σ confidence interval derived from the posterior distribution.

with the other data points, we exclude the 1.155 and 1.199 μm data points in the subsequent retrieval analysis.

In addition to the HST measurements, two ground-based secondary-eclipse measurements of WASP-33 b have been reported in the literature: a 0.9 μm data point from Smith et al. (2011) and a Ks-band measurement from Deming et al. (2012). The 0.9 μm measurement is not included in our joint retrieval because the transmission curve of the filter used in that observation is not available, preventing a self-consistent modeling within *petitRADTRANS*. The Ks-band eclipse measurement, by contrast, can be readily incorporated. We therefore performed additional retrievals including this data point and find that the inferred atmospheric parameters remain fully consistent with our

Table 3: Bayesian model comparison of the chemical species considered for the Free model

Species	$\Delta \ln(\mathcal{Z})$	Inferences
H_2O	-0.3	Inconclusive
CO	0.1	Inconclusive
CH_4	-0.2	Inconclusive
H^-	71.3	Strong
TiO	-0.5	Inconclusive

Notes. The logarithmic Bayesian evidence, calculated as $\ln(\mathcal{Z}_{\text{full}}) - \ln(\mathcal{Z}_{\text{no-X}})$, quantifies the statistical preference for excluding a certain species X in the atmospheric model, with uncertainties of 0.7. The species in bold possess strong evidence.

nominal results, with all differences well within the 1σ uncertainties. This demonstrates that our conclusions are insensitive to the inclusion of the Ks-band measurement; consequently, it is not included in the final retrieval presented here.

The best-fit result for the FREE model is shown in Fig.12, with Figs.13 & Table 2 illustrating the corresponding mass mixing ratios (MMRs) and T-P profile. Table 3 reports the detection significance represented by the Bayesian evidence for each chemical species.

In the FREE retrieval, WASP-33 b's dayside atmosphere exhibits a strong temperature inversion layer and a featureless emission spectrum, resulting in no or very poor constraints on the MMRs for all the considered species except H^- and e^- , which have quite high concentrations. Lacking concrete detection of molecules is in line with the LR space-based results from Changeat et al. (2022), but seems to conflict with the HR results (Finnerty et al. 2023). The results may be caused by: (1) High temperatures in the emission-contribution layers thermally dissociate most molecules and thus reduce their detectability; (2) Residual pulsation noise in the HST spectra could still obscure molecular features, even after correction; (3) the feature-

Table 4: Best-fit parameters from the EQ model retrieval on WASP-33 b

Parameter	Prior	Posterior distribution	Unit
T_1	$\mathcal{U}(1000, 3000)$	2034 ± 338	K
T_2	$\mathcal{U}(3000, 5000)$	4849 ± 149	K
T_3	$\mathcal{U}(1000, 3000)$	2646 ± 379	K
P_1	$\mathcal{U}(-2, 3)$	-1.16 ± 0.35	log bar
P_2	$\mathcal{U}(-6, -2)$	-2.46 ± 0.24	log bar
P_3	-6	...	log bar
[Fe/H]	$\mathcal{U}(-1, 3)$	1.51 ± 0.44	dex
C/O	$\mathcal{U}(0.1, 1.6)$	0.783 ± 0.032	dex

less spectrum forces the retrieval to fit continuum opacity by the inclusion of a large amount of H^- .

The EQ retrieval analysis yields consistent results with those from the HR spectroscopic study (Changeat et al. 2022). The best-fit model spectrum, the corresponding T-P profile and the pressure-dependent chemical abundances are presented in Fig.14, Fig. 15 and Table 4, respectively. The retrieved T-P profile suggests that the temperature inversion layer initiates near 1 bar, consistent with previous results (e.g. Nugroho et al. 2021; van Sluijs et al. 2023; Finnerty et al. 2023), though the layer above the inversion is relatively cooler in our results. As shown in Table 4, the dayside atmosphere of WASP-33 b should be highly metal-rich and exhibit a super-solar C/O ratio.

Table 5 summarizes the Bayesian-evidence validation for each species, showing strong support for H^- , H_2O , and CO , weak support for TiO , and no support for CH_4 . Figure 16 displays the mass mixing ratios (MMRs) of these species as a function of pressure derived from the retrieved T-P profile. Given that CH_4 is disfavored by the Bayesian evidence and is thermochemically implausible in the dayside atmosphere of UHJs, we therefore do not further examine the CH_4 MMR. Although the H^- abundance in the EQ model is appreciably lower than in the FREE model, the strong Bayesian evidence for H^- in both frameworks underscores its necessity in the dayside atmosphere. The very high, nearly constant MMR of CO with altitude, together with the comparatively lower abundance of H_2O , is consistent with the KPIC detection reported by Finnerty et al. (2023). The low concentration of TiO is likely a natural consequence of thermal dissociation in the hot upper atmosphere. Note that the retrieved emission spectrum is dominated by atmospheric layers between 1 μ bar and 1 bar; therefore the species abundances within this pressure range are expected to be the most reliable.

4.2. EQ model retrieval

In conventional planet formation theories like pebble accretion (Ormel & Klahr 2010; Lambrechts & Johansen 2012), metallicity and the C/O ratio generally show an inverse correlation, making it unlikely for planets to simultaneously possess both high C/O ratio and high metallicity. However, the pebble drift theory proposed by Booth et al. (2017) indicates that the metallicity of planets can be enriched not only by accreting solids but also by accreting metal-rich gas generated through pebble drift mechanism. Synthesizing the dynamical and chemical properties of WASP-33 b, our conclusions align with those

Table 5: Bayesian model comparison of the chemical species retrieved with EQ model

Species	$\Delta \ln(\mathcal{Z})$	Inferences
H_2O	25.7	Strong
CO	36	Strong
CH_4	-0.1	Inconclusive
H^-	147.6	Strong
TiO	2.5	Weak

Notes. Same as Table.3, with uncertainties of ~ 0.2 .

outlined in Finnerty et al. (2023): the planet likely formed in a carbon- and solid-rich zone with high C/O ratio, such as near the CO_2 snowline (~ 10 au for an A-type primary star (Öberg et al. 2011; Mollière et al. 2022)), accreted a high-metallicity atmosphere from its vicinity, and migrated to its present location via a process like eccentric *Lidov-Kozai* effect (Naoz et al. 2011). It should be noted, as suggested by Finnerty et al. (2023), that the observed high C/O ratio in the dayside atmosphere could also be biased by data interpretation, namely by the weak constraints on oxygen-bearing species. For example, our retrieval lacks constraints on OH , a photodissociation product of H_2O . Given that significant amount of H_2O should be photodissociated into OH in upper atmospheres, this lack may lead to an overestimated C/O ratio.

On the other hand, using only metallicity and C/O ratio as diagnostics is insufficient to accurately or unbiasedly constrain planet formation and evolution history (Feinstein et al. 2025). Incorporating measurements of additional tracers (e.g., volatile elements and refractory element abundances) would better enrich the understanding of WASP-33 b's formation history. We recommend future JWST observations of WASP-33 b to achieve more precise atmospheric constraints.

5. Summary and Conclusion

We conducted two secondary-eclipse observations of the ultra-hot Jupiter WASP-33 b with CFHT/WIRCam to constrain the planet's dayside atmosphere. To handle the thousands of iterations required for systematics correction and atmospheric retrievals, we developed a parallelized data reduction and analysis pipeline, which substantially reduced computational time. After carefully removing the host star's pulsation noise, we measured eclipse depths of $1565.2^{+228.6}_{-237.5}$ ppm in the CO filter and $914.3^{+56.1}_{-57.0}$ ppm in the CH_4_{on} filter.

In addition to our CFHT/WIRCam observations, we incorporated HST/WFC3 spectroscopic data (Haynes et al. 2015) and Spitzer/IRAC photometric measurements ($3.6 \mu m$ (Zhang et al. 2018), $4.5 \mu m$ (Dang et al. 2024)) to jointly perform both free-chemistry and equilibrium-chemistry atmospheric retrievals using *petitRADTRANS*. Given the extreme dayside temperatures typical of ultra-hot Jupiters, we consider the equilibrium-chemistry model to be a more physically representative description of WASP-33 b's dayside atmosphere, comparing to the free chemistry model. Accordingly, all results presented in the main findings below are based on the equilibrium model. Our main findings are summarized as follows:

1. Thermal inversion and opacity sources. WASP-33 b exhibits a clear thermal inversion from both free and equilibrium retrievals. Under the free-chemistry model, the dayside emission

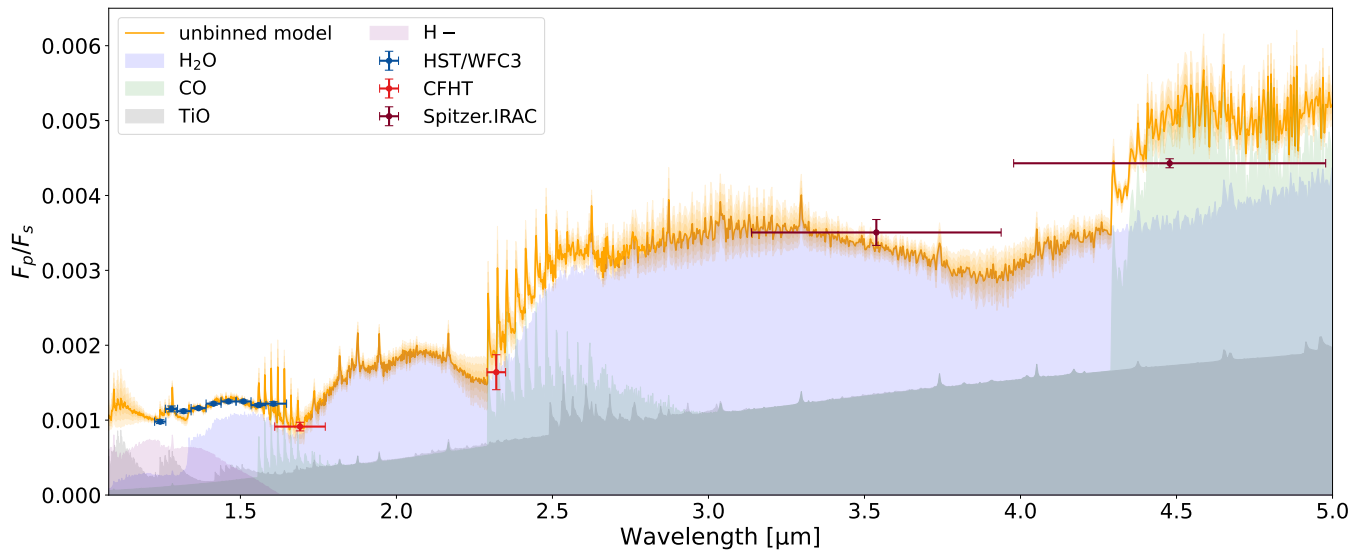


Fig. 14: Same as Fig. 12, but for the EQ retrieval. Note that H_2O , H^- , and CO all exhibit prominent features in the model spectrum.

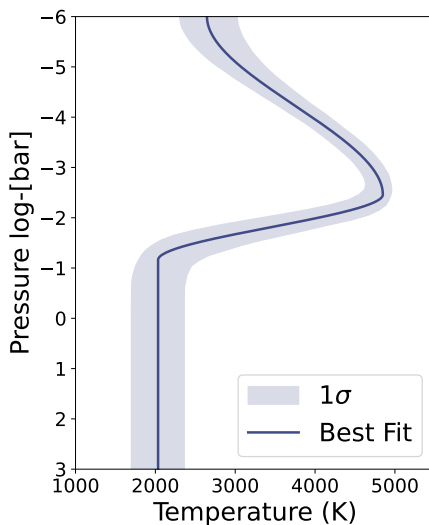


Fig. 15: Retrieved T-P profile from the EQ model. Same as Fig.13.

spectrum appears largely featureless, with Bayesian evidence strongly favoring the presence of H^- opacity. However, the retrieved abundances of H^- and e^- are considered unreliable due to model limitations and spectral coverage. Incorporating blue or optical spectra in future joint retrievals will better constrain these species.

2. High C/O ratio and metallicity under equilibrium chemistry. The equilibrium-chemistry retrieval yields a high C/O ratio of $0.78^{+0.03}_{-0.04}$ and a metallicity of $\sim 26 \times$ stellar, both more precisely constrained than in previous studies. The emission spectrum is primarily shaped by H_2O , CO , and H^- , while the existence of TiO remains uncertain due to weak Bayesian evidence. In the upper atmosphere, most molecules undergo thermal dissociation except CO .

3. Formation and migration implications. The combination of high metallicity and high C/O ratio is consistent with planetary enrichment through the accretion of metal-rich gas, as proposed by the pebble drift theory (Booth et al. 2017). A possi-

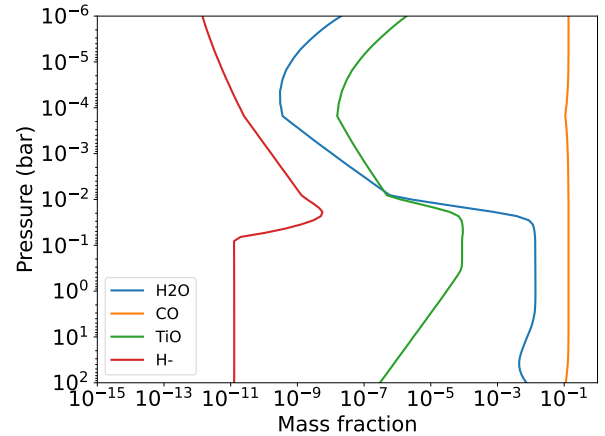


Fig. 16: Mass mixing ratios of chemical species under EQ model as functions of atmospheric height. Apart from CO maintaining high concentrations and H^- exhibiting a marked increase with rising temperature, all other molecules undergo thermal dissociation within the thermal inversion layer.

ble formation and migration scenario suggests that WASP-33 b formed and/or accreted material in a carbon- and solid-rich region — possibly near the CO_2 snow line — before migrating inward via a mechanism such as the eccentric Lidov–Kozai effect (Naoz et al. 2011). To test this hypothesis and rule out apparent carbon enrichment caused by weak constraints on oxygen-bearing species, we recommend follow-up JWST observations to obtain tighter constraints on additional elemental abundances.

WASP-33 b remains an unusual exoplanet, orbiting a δ Scuti variable star. Its high metallicity, elevated C/O ratio, and misaligned orbit together indicate a distinct formation and evolutionary history. Although stellar pulsations previously posed major challenges for measuring transit and eclipse depths, improved methodologies now allow for better mitigation of these signals and stronger isolation of the planetary component. Future observations — either at higher spectral resolution in targeted bands or with broader wavelength coverage at lower resolution — will en-

able more detailed characterization of WASP-33 b's atmosphere and provide deeper insight into its formation and evolution.

Acknowledgements. We thank the referee and editor for their concise review and instructive suggestion. This research is supported by the National Key R&D Program of China (2025YFE0102100, 2024YFA1611802, 2025YFE0213204), the National Natural Science Foundation of China under grant 62127901, 12588202, National Astronomical Observatories Chinese Academy of Sciences No. E4TQ2101, and the Pre-research project on Civil Aerospace Technologies No. D010301 funded by the China National Space Administration (CNSA), by the China Manned Space Program with grant no. CMS-CSST-2025-A16. We acknowledge financial support from the Agencia Estatal de Investigación of the Ministerio de Ciencia e Innovación MCIN/AEI/10.13039/501100011033 and the ERDF 'A way of making Europe' through projects PID2021-125627OB-C32 and PID2024-158486OB-C32. MZ was supported by the Chinese Academy of Sciences (CAS), through a grant to the CAS South America Center for Astronomy (CASSACA) in Santiago, Chile. This research uses data obtained through the Telescope Acess Program(TAP), which has been funded by the National Astronomical Observatories of China, the Chinese Academy of Sciences, and the Special Fund for Astronomy from the Ministry of Finance. Two nights (Oct 25 & Dec 24,2015) with WIRCam on the 3.6m CFHT telescope were distributed to us for scientific studies of exoplanetary atmosphere via the TAP. We also thank Dr. Jie Zheng, Jingyuan Zhao, Hengkai Ding and Yingjie Cai for their constructive comments on this work.

References

Anderson, D. R., Temple, L. Y., Nielsen, L. D., et al. 2018, arXiv e-prints, arXiv:1809.04897

Baluev, R. V. & Sokov, E. N. 2025, MNRAS, 537, 171

Baxter, C., Désert, J.-M., Parmentier, V., et al. 2020, A&A, 639, A36

Booth, R. A., Clarke, C. J., Madhusudhan, N., & Ilee, J. D. 2017, MNRAS, 469, 3994

Bradley, L., Sipőcz, B., Robitaille, T., et al. 2024, astropy/photutils: 1.11.0

Buchner, J., Georgakakis, A., Nandra, K., et al. 2014, A&A, 564, A125

Cabot, S. H., Bello-Arufe, A., Mendonça, J. M., et al. 2021, AJ, 162, 218

Cabot, S. H., Madhusudhan, N., Welbanks, L., Piette, A., & Gandhi, S. 2020, MNRAS, 494, 363

Chakrabarty, A. & Sengupta, S. 2019, AJ, 158, 39

Changeat, Q., Edwards, B., Al-Refaie, A. F., et al. 2022, ApJS, 260, 3

Chen, G., van Boekel, R., Wang, H., et al. 2014, A&A, 563, A40

Christian, D. J., Pollacco, D., Skillen, I., et al. 2006, MNRAS, 372, 1117

Cont, D., Yan, F., Reiners, A., et al. 2021, A&A, 651, A33

Cont, D., Yan, F., Reiners, A., et al. 2022, A&A, 668, A53

Cont, D., Yan, F., Reiners, A., et al. 2022, A&A, 657, L2

Cridland, A. J., Eistrup, C., & van Dishoeck, E. F. 2019, A&A, 627, A127

Croll, B., Albert, L., Jayawardhana, R., et al. 2015, ApJ, 802, 28

Croll, B., Albert, L., Lafreniere, D., Jayawardhana, R., & Fortney, J. J. 2010, ApJ, 717, 1084

Cutri, R., Skrutskie, M., Van Dyk, S., et al. 2003, VizieR Online Data Catalog, 2246, II

Dang, L., Bell, T. J., Shu, Y. Z., et al. 2024, AJ, 169, 32

De Mooij, E., Brogi, M., De Kok, R., et al. 2013, A&A, 550, A54

Delrez, L., Santerne, A., Almenara, J. M., et al. 2016, MNRAS, 458, 4025

Deming, D., Fraire, J. D., Sada, P. V., et al. 2012, ApJ, 754, 106

Devost, D., Albert, L., Teeple, D., & Croll, B. 2010, in SPIECS, Vol. 7737, Observatory Operations: Strategies, Processes, and Systems III, ed. D. R. Silva, A. B. Peck, & B. T. Soifer, 77372D

Ding, H., Shu, Y., Chen, Y., et al. 2025, RAA, 25, 065013

Drummond, B., Carter, A. L., Hébrard, E., et al. 2019, MNRAS, 486, 1123

Espinosa, N., Fortney, J. J., Miguel, Y., Thorngren, D., & Murray-Clay, R. 2017, ApJ, 838, L9

Evans-Soma, T. M., Sing, D. K., Barstow, J. K., et al. 2025, Nat. Astron., 1

Everett, M. E. & Howell, S. B. 2001, PASP, 113, 1428

Feinstein, A. D., Booth, R. A., Bergner, J. B., et al. 2025, arXiv preprint arXiv:2506.00669

Feroz, F., Hobson, M., & Bridges, M. 2009, MNRAS, 398, 1601

Finger, G., Dorn, R. J., Eschbaumer, S., et al. 2008, in High Energy, Optical, and Infrared Detectors for Astronomy III, Vol. 7021, SPIE, 236–248

Finnerty, L., Schofield, T., Sappey, B., et al. 2023, AJ, 166, 31

Foreman-Mackey, D. 2018, RNAAS, 2, 31

Foreman-Mackey, D., Agol, E., Ambikasaran, S., & Angus, R. 2017, AJ, 154, 220

Foreman-Mackey, D., Hogg, D. W., Lang, D., & Goodman, J. 2013, PASP, 125, 306

Gaia Collaboration. 2020, VizieR Online Data Catalog, 1350, I

Gandhi, S., Kesseli, A., Zhang, Y., et al. 2023, AJ, 165, 242

Gaudi, B. S., Stassun, K. G., Collins, K. A., et al. 2017, Nature, 546, 514

Grenier, S., Baylac, M.-O., Rolland, L., et al. 1999, A&AS, 137, 451

Haynes, K., Mandell, A. M., Madhusudhan, N., Deming, D., & Knutson, H. 2015, ApJ, 806, 146

Herman, M. K., de Mooij, E. J., Nugroho, S. K., Gibson, N. P., & Jayawardhana, R. 2022, AJ, 163, 248

Herman, M. K., de Mooij, E. J. W., Jayawardhana, R., & Brogi, M. 2020, AJ, 160, 93

Hoeijmakers, H., Kitzmann, D., Morris, B., et al. 2024, A&A, 685, A139

Johnson, M. C., Cochran, W. D., Collier Cameron, A., & Bayliss, D. 2015, ApJ, 810, L23

Kass, R. E. & Raftery, A. E. 1995, JASA, 90, 773

Kreidberg, L. 2015, PASP, 127, 1161

Lambrechts, M. & Johansen, A. 2012, A&A, 544, A32

Lendl, M., Csizmadia, S., Deline, A., et al. 2020, A&A, 643, A94

Madhusudhan, N. 2012, ApJ, 758, 36

McKemmish, L. K., Masseron, T., Hoeijmakers, H. J., et al. 2019, MNRAS, 488, 2836

Mollière, P., Molyarova, T., Bitsch, B., et al. 2022, ApJ, 934, 74

Mollière, P., van Boekel, R., Dullemond, C., Henning, T., & Mordasini, C. 2015, ApJ, 813, 47

Mollière, P., Wardenier, J., Van Boekel, R., et al. 2019, A&A, 627, A67

Moses, J., Madhusudhan, N., Visscher, C., & Freedman, R. 2012, ApJ, 763, 25

Moya, A., Bouy, H., Marchis, F., Vicente, B., & Barrado, D. 2011, A&A, 535, A110

Mraz, G., Darveau-Bernier, A., Boucher, A., et al. 2024, ApJ, 975, L42

Mugrauer, M. 2019, MNRAS, 490, 5088

Naoz, S., Farr, W. M., Lithwick, Y., Rasio, F. A., & Teyssandier, J. 2011, Nature, 473, 187

Nasedkin, E., Mollière, P., & Blain, D. 2024, The Journal of Open Source Software, 9, 5875

Ngo, H., Knutson, H. A., Hinkley, S., et al. 2016, ApJ, 827, 8

Nugroho, S. K., Gibson, N. P., de Mooij, E. J. W., et al. 2020, ApJ, 898, L31

Nugroho, S. K., Kawahara, H., Gibson, N. P., et al. 2021, ApJ, 910, L9

Nugroho, S. K., Kawahara, H., Masuda, K., et al. 2017, AJ, 154, 221

Öberg, K. I., Murray-Clay, R., & Bergin, E. A. 2011, ApJ, 743, L16

Ormel, C. & Klahr, H. 2010, A&A, 520, A43

Parmentier, V., Line, M. R., Bean, J. L., et al. 2018, A&A, 617, A110

Pollacco, D. L., Skillen, I., Cameron, A. C., et al. 2006, PASP, 118, 1407

Rothman, L. S., Gordon, I., Barber, R., et al. 2010, Journal of Quantitative Spectroscopy and Radiative Transfer, 111, 2139

Rubenzahl, R. A., Dai, F., Halverson, S., et al. 2024, AJ, 168, 188

Serindag, D. B., Nugroho, S. K., Mollière, P., et al. 2021, A&A, 645, A90

Sheppard, K. B., Mandell, A. M., Tamburo, P., et al. 2017, ApJ, 850, L32

Shi, Y., Wang, W., Zhao, G., et al. 2023, MNRAS, 522, 1491

Smith, A., Anderson, D., Skillen, I., Cameron, A. C., & Smalley, B. 2011, MNRAS, 416, 2096

Smith, P. C. B., Sanchez, J. A., Line, M. R., et al. 2024, AJ, 168, 293

Snellen, I. A. 2025, ARA&A, 63

Stangret, M., Casasayas-Barris, N., Pallé, E., et al. 2022, A&A, 662, A101

Stangret, M., Pallé, E., Casasayas-Barris, N., et al. 2021, A&A, 654, A73

Stassun, K. G., Oelkers, R. J., Paegert, M., et al. 2019, AJ, 158, 138

Stephan, A. P., Wang, J., Cauley, P. W., et al. 2022, ApJ, 931, 111

Stolker, T., Quanz, S. P., Todorov, K. O., et al. 2020, A&A, 635, A182

Tan, X., Komacek, T. D., Batalha, N. E., et al. 2024, MNRAS, 528, 1016

van Sluijs, L., Birkby, J. L., Lothringer, J., et al. 2023, MNRAS, 522, 2145

von Essen, C., Czesla, S., Wolter, U., et al. 2014, A&A, 561, A48

Von Essen, C., Mallonn, M., Borre, C., et al. 2020, A&A, 639, A34

von Essen, C., Mallonn, M., Welbanks, L., et al. 2019, A&A, 622, A71

Waldmann, I. P., Rocchetto, M., Tinetti, G., et al. 2015, ApJ, 813, 13

Wang, W., van Boekel, R., Madhusudhan, N., et al. 2013, ApJ, 770, 70

Watanabe, N., Narita, N., Pallé, E., et al. 2022, MNRAS, 512, 4404

Winn, J. N., Holman, M. J., Torres, G., et al. 2008, ApJ, 683, 1076

Wöllert, M. & Brandner, W. 2015, A&A, 579, A129

Yan, F. & Henning, T. 2018, Nat. Astron., 2, 714

Yan, F., Pallé, E., Reiners, A., et al. 2022, A&A, 661, L6

Yan, F., Wyttenbach, A., Casasayas-Barris, N., et al. 2021, A&A, 645, A22

Yang, Y., Chen, G., Wang, S., & Yan, F. 2024a, AJ, 167, 36

Yang, Y., Chen, G., Yan, F., Tan, X., & Ji, J. 2024b, ApJ, 971, L8

Yurchenko, S. N., Amundsen, D. S., Tennyson, J., & Waldmann, I. P. 2017, A&A, 605, A95

Zhang, M., Knutson, H. A., Kataria, T., et al. 2018, AJ, 155, 83